

Cite this: *Phys. Chem. Chem. Phys.*,
2015, 17, 166

Direct observation of key photoinduced dynamics in a potential nano-delivery vehicle of cancer drugs

Samim Sardar,^a Siddhi Chaudhuri,^a Prasenjit Kar,^a Soumik Sarkar,^a Peter Lemmens^{bc} and Samir Kumar Pal^{*a}

In recent times, significant achievements in the use of zinc oxide (ZnO) nanoparticles (NPs) as delivery vehicles of cancer drugs have been made. The present study is an attempt to explore the key photoinduced dynamics in ZnO NPs upon complexation with a model cancer drug protoporphyrin IX (PP). The nanohybrid has been characterized by FTIR, Raman scattering and UV-Vis absorption spectroscopy. Picosecond-resolved Förster resonance energy transfer (FRET) from the defect mediated emission of ZnO NPs to PP has been used to study the formation of the nanohybrid at the molecular level. Picosecond-resolved fluorescence studies of PP-ZnO nanohybrids reveal efficient electron migration from photoexcited PP to ZnO, eventually enhancing the ROS activity. The dichlorofluorescein (DCFH) oxidation and no oxidation of luminol in PP/PP-ZnO nanohybrids upon green light illumination unravel that the nature of ROS is essentially singlet oxygen rather than superoxide anions. Surface mediated photocatalysis of methylene blue (MB) in an aqueous solution of the nanohybrid has also been investigated. Direct evidence of the role of electron transfer as a key player in enhanced ROS generation from the nanohybrid is also clear from the photocurrent measurement studies. We have also used the nanohybrid in a model photodynamic therapy application in a light sensitized bacteriological culture experiment.

Received 21st August 2014,
Accepted 28th October 2014

DOI: 10.1039/c4cp03749a

www.rsc.org/pccp

1. Introduction

The use of nanoscale materials in delivering drugs precisely and safely to the target site at the right time and with maximum impact provides a great opportunity in the area of drug delivery. These nanoscale materials facilitate high drug loading due to their large surface to volume ratio and consequently minimize the toxicity by their preferential accumulation at the target site. Nanoparticle-based drug delivery systems have many other advantages such as improving the solubility of hydrophobic drugs and also prolonging the half-life of systemic circulation of drugs by reducing immunogenicity.^{1,2} A number of nanoparticle-based therapeutic and diagnostic agents have been successfully introduced in the treatment of diabetes, pain, cancer and infectious diseases.^{3–8} However, most of the nanoparticles are toxic to animals and very less biocompatible *in vivo*.^{9–11} Among them ZnO nanoparticles (NPs) have shown promising potential

as drug delivery vehicles due to their low cost, good biocompatibility and low toxicity.^{12–14} Unfortunately, because of its large band gap of 3.3 eV, the popular ZnO can be activated only by UV light of wavelength < 375 nm. UV light is not suitable for most *in vivo* experiments because it can only penetrate the skin by several millimeters and is harmful to the human body. However, ZnO NPs as efficient drug carriers in photodynamic therapies (PDT) which avoid non-significant accumulation of the drug at the target site have attracted considerable research interest.¹⁵

PDT is a promising noninvasive treatment for cancer which involves the uptake of a photosensitizer by cancer tissue followed by photoirradiation.^{16–18} Protoporphyrin IX (PP) is a very well-known cancer drug and efficient hydrophobic photosensitizer (PS) for PDT.¹⁹ The efficiency of PDT depends on the photoactivation of the photosensitizers accumulated at the target site and the pharmacokinetic properties of the photosensitizer to achieve the desired biological response. Due to the very low water solubility of hydrophobic drugs like PP, several strategies have been employed to prepare stable formulations, including conjugation to water-soluble polymers or encapsulation in colloidal carriers such as oil-in-water emulsions,²⁰ gold nanoparticles,^{21,22} polymer nanoparticles,^{23,24} microspheres²⁵ and block copolymer micelles.^{26,27} Majid and coworkers¹⁵ have

^a Department of Chemical, Biological and Macromolecular Sciences, S. N. Bose National Centre for Basic Sciences, Block JD, Sector III, Salt Lake, Kolkata 700 098, India. E-mail: skpal@bose.res.in; Fax: +91 033 2335 3477; Tel: +91 033 2335 5706-08

^b Institute for Condensed Matter Physics, TU Braunschweig, Mendelssohnstraße 3, 38106 Braunschweig, Germany

^c Laboratory for Emerging Nanometrology, TU Braunschweig, Germany

shown that PEGylated ZnO NPs coated with PP exhibit an excellent anticancer effect due to countable localization of the drug in the targeted area in the presence of a suitable light dose. ZnO NPs loaded with drugs can penetrate cancer cells through specific ligand–receptor recognition or non-specific binding forces based on hydrophobic or coulombic interactions.¹² The stability of the combination of the ZnO and the drug molecules is very important. The guest drug molecules should not leak from the host surface during blood circulation *in vivo*, so strong interactions with ZnO carriers are necessary, *e.g.*, covalent bonds. The drug molecules have to be released from these carriers easily at the target site. The tumor and cancer cells have acidic environments and ZnO NPs are decomposed completely at pH 5 in aqueous solution, therefore drugs can be released easily by ZnO nanocarriers at the target site.²⁸

The photochemical and photophysical processes in the PS during PDT are key to the generation of reactive oxygen species (ROS). When a PS in its ground state is exposed to light of a specific wavelength, it absorbs a photon and is promoted to an excited singlet state. The singlet state is eventually decayed to the triplet excited state *via* intersystem crossing (ISC) and then the triplet state energy is transferred to ground state molecular oxygen to produce singlet oxygen. It is the cytotoxicity of the singlet oxygen which can cause oxidation of biomolecules and, finally, cell death. The enhancement in the ROS generation can essentially increase the overall activity of a PS, thereby reducing the concentration of the essential photosensitizer. Therefore, the electron–hole separation in a PS, immediately after the photo-excitation, is a key step to enhance the average ROS concentration. In this context, photoinduced electron transfer between drugs and colloidal semiconductors plays a vital role where the rapid charge injection from sensitizer molecules to the conduction band (CB) of the semiconductor followed by the generation of ROS may enhance the activity of the PS. This necessitates the exploration of photoinduced ultrafast dynamics in the PP–ZnO nanohybrid as a potential photodynamic agent.

In the present study, our aim is to explore the key photo-induced dynamics in ZnO upon complexation with a model cancer drug PP, which eventually leads to enhanced efficiency in PDT and successful realization of ZnO NPs as the drug delivery vehicle of cancer drugs. The nanohybrid was characterized by UV-Vis absorption spectroscopy, Vibrational spectroscopy (FTIR) and Raman scattering. To study the nanohybrid formation at the molecular level, picosecond-resolved Förster resonance energy transfer (FRET) from the defect emission of ZnO to PP has been used. Picosecond-resolved fluorescence studies on the PP–ZnO nanohybrid also reveal efficient electron migration from photo-excited PP to ZnO, eventually enhancing the ROS activity in the PP–ZnO nanostructures. In addition, we have used a well-known electron acceptor, *p*-benzoquinone (BQ), to emphasize the electron-donating efficiency of PP upon photo-excitation. Our studies on ROS markers including dichlorofluorescein (DCFH) and luminol in aqueous PP/PP–ZnO nanohybrid solution upon green light illumination unravel the nature of ROS. PP–ZnO nanohybrids were employed to construct photo-active electrodes that lead to an enhanced photocurrent.

We have also used the nanohybrid in a model photodynamic therapy application in light sensitized bacteriological culture experiments.

2. Experimental section

Analytical grade chemicals were used for synthesis without further purification. 30 nm ZnO NPs were obtained from Sigma-Aldrich. Solutions of protoporphyrin IX (PP, obtained from Sigma) and *p*-benzoquinone (BQ, from Fluka) were prepared in dimethyl sulfoxide (DMSO, from Spectrochem). Conductive fluorine-doped tin oxide (FTO) coated glass substrates (from Sigma-Aldrich) were cleaned by successive sonication with soap water, acetone, ethanol and deionized (DI) water for 15 min each with adequate drying prior to their use.

2.1. Synthesis of ZnO NPs

ZnO NPs were synthesized in a colloidal solution using ethanol, C₂H₅OH (Merck), as the solvent. The coprecipitation technique has been reported in previous publications from our group.^{29–31} Briefly, 20 mL of 4 mM zinc acetate dihydrate solution, (CH₃COO)₂Zn·2H₂O (Merck), was heated at 70 °C for 30 min. 20 mL of 4 mM sodium hydroxide solution, NaOH (Merck), in ethanol was then added and the mixture was hydrolyzed for 2 h at 60 °C to obtain NPs of average diameters of ~5 nm.

2.2. Sensitization of PP on the ZnO NPs surface

A 0.5 mM PP solution, C₃₄H₃₆N₄O₅, was prepared in a dimethyl sulfoxide (DMSO)–deionized (DI) water (v/v) mixture under constant stirring for 1 h. The sensitization of ZnO NPs with PP dye was carried out at room temperature in the dark by adding ZnO NPs into a 0.5 mM PP solution with continuous stirring for 12 h. After the sensitization process, the solution was centrifuged for a few minutes and the supernatant clear solution of unattached dyes was removed. Then the sensitized material was washed with a DMSO–water mixture several times to remove any unattached dye. The nanohybrid was then dried in a water bath and stored in the dark until further use.

2.3. Synthesis of ZnO NRs

Zinc acetate dihydrate, Zn(CH₃COO)₂·2H₂O (Merck), zinc nitrate hexahydrate, Zn(NO₃)₂·6H₂O (Sigma-Aldrich), and hexamethylenetetramine, C₆H₁₂N₄ (Aldrich), were used as the starting materials for a low temperature hydrothermal synthesis of ZnO NRs on FTO substrates. Detailed processes for the hydrothermal growth of single crystalline ZnO NRs are described in our previous reports.^{32,33} In brief, a ZnO seed layer was initially deposited on cleaned FTO substrates by the spray-pyrolysis method at 350 °C using 10 mM zinc acetate aqueous solution. The seeded FTO substrates were then annealed in air at 350 °C for 1 h and used for the hydrothermal growth of the ZnO NRs. An aqueous solution of zinc nitrate (20 mM) and hexamethylenetetramine (20 mM) was used as the precursor solution for the ZnO NR growth, which was carried out at 90 °C for 40 h. This led to the growth of ZnO NRs of length *ca.* 3–4 μm and a diameter

of 80–100 nm.^{32,34} During the hydrothermal process, in order to maintain a constant growth rate of the ZnO NRs, the old precursor solution was replaced with a fresh solution every 5 h. As-obtained ZnO NR samples were then taken out of the reaction vessel and rinsed thoroughly with DI water to remove unreacted residues. Finally, the samples were annealed in air at 350 °C for 1 h prior to the study.

2.4. Characterization methods

Transmission electron microscopy (TEM) grids were prepared by applying a diluted drop of the ZnO samples to carbon-coated copper grids. The particle sizes were determined from micrographs recorded at a magnification of 100 000 \times using an FEI (Technai S-Twin, operating at 200 kV) instrument. For optical experiments, the steady-state absorption and emission were determined using a Shimadzu UV-2450 spectrophotometer and a Jobin Yvon Fluoromax-3 fluorimeter respectively. Picosecond-resolved spectroscopic studies were done using a commercial time correlated single photon counting (TCSPC) setup from Edinburgh Instruments (instrument response function (IRF) = 80 ps), excitation at 375 nm and 409 nm). The observed fluorescence transients were fitted by using a nonlinear least square fitting procedure to a function

$$\left(X(t) = \int_0^t E(t')R(t-t')dt' \right) \quad (1)$$

comprising of convolution of the IRF ($E(t)$) with a sum of exponentials

$$\left(R(t) = A + \sum_{i=1}^N B_i e^{-t/\tau_i} \right) \quad (2)$$

with pre-exponential factors (B_i), characteristic lifetimes (τ_i) and a background (A). The relative concentration in a multi-exponential decay is finally expressed as

$$c_n = \frac{B_n}{\sum_{i=1}^N B_i} \times 100 \quad (3)$$

and the average lifetime (amplitude-weighted) of a multi-exponential decay is expressed as

$$\tau_{av} = \sum_{i=1}^N c_i \tau_i \quad (4)$$

The FTIR spectra were recorded on a JASCO FTIR-6300 spectrometer, using a CaF₂ window. Raman scattering measurements were performed by using a LabRAM HR JobinYvon system fitted with a Peltier-cooled charge-coupled device (CCD) detector. An air cooled argon ion laser with a wavelength of 488 nm was used as the excitation light source. DLS measurements were performed using a Nano S Malvern instrument employing a 4 mW He-Ne laser ($\lambda = 632.8$ nm) equipped with a thermostated sample chamber. All the scattered photons are collected at a 173° scattering angle. The scattering intensity data are processed using the instrumental software to obtain the hydrodynamic diameter (d_H) and the size distribution of the scatterer in each sample. The instrument measures the time dependent fluctuation in

the intensity of light scattered from the particles in solution at a fixed scattering angle. d_H is defined as:

$$d_H = \frac{k_B T}{3\pi\eta D} \quad (5)$$

where k_B is the Boltzmann constant, T is the temperature, η is the viscosity, and D is the translational diffusion coefficient. In a typical size distribution graph from the DLS measurement, the X -axis shows a distribution of size classes in nanometers, while the Y -axis shows the relative intensity of the scattered light.

We have studied the complexation between PPIX and different concentrations of the well-known electron acceptor BQ. The ratio of the timescales of PPIX in the absence (τ_0) and presence (τ) of the quencher BQ can be expressed by the Stern–Volmer equation:

$$\frac{\tau_0}{\tau} = 1 + K_D [Q] \quad (6)$$

where τ_0/τ is the relative excited-state lifetime, and K_D is the dynamic quenching constant.³⁵

2.5. Förster resonance energy transfer (FRET) calculations

In order to estimate FRET efficiency of the donor (ZnO) and hence to determine the distance of donor–acceptor pairs, we used the following methodology.³⁵ The Förster distance (R_0) is given by

$$R_0 = 0.211 \times [\kappa^2 n^{-4} Q_D J]^{1/6} \text{ (in } \text{Å}) \quad (7)$$

where κ^2 is a factor describing the relative orientation in space of the transition dipoles of the donor and acceptor. For donors and acceptors that randomize by rotational diffusion prior to energy transfer, the magnitude of κ^2 is assumed to be 2/3. The refractive index (n) of the medium is assumed to be 1.496. Q_D , the integrated quantum yield of the donor in the absence of the acceptor, is measured to be 3.8×10^{-3} . J , the overlap integral, which expresses the degree of spectral overlap between the donor emission and the acceptor absorption, is given by

$$J(\lambda) = \frac{\int_0^\infty F_D(\lambda) \epsilon_A(\lambda) \lambda^4 d\lambda}{\int_0^\infty F_D(\lambda) d\lambda} \quad (8)$$

where $F_D(\lambda)$ is the fluorescence intensity of the donor in the wavelength range of λ to $\lambda + d\lambda$ and is dimensionless; $\lambda_A(\lambda)$ is the extinction coefficient (in $M^{-1} \text{ cm}^{-1}$) of the acceptor at λ . If λ is in nm, then J is in units of $M^{-1} \text{ cm}^{-1} \text{ nm}^4$. The estimated value of the overlap integral is 2.50×10^{15} . Once the value of R_0 is known, the donor–acceptor distance (r_{DA}) can be easily calculated using the formula

$$r_{DA}^6 = \frac{[R_0^6(1-E)]}{E} \quad (9)$$

Here E is the efficiency of energy transfer. The transfer efficiency is measured using the relative fluorescence lifetime of the donor, in the absence (τ_D) and presence (τ_{DA}) of the acceptor.

$$E = 1 - \frac{\tau_{DA}}{\tau_D} \quad (10)$$

From the average lifetime calculation for the PP-ZnO nano-hybrids, we obtained the effective distance between the donor and the acceptor (r_{DA}), using eqn (9) and (10).

2.6. Materials and methods for the VLP process

For the photocatalysis study, ZnO and PP-ZnO nanohybrids were dispersed in DI water, and aqueous solution of MB in DI water was used as a test contaminant. A 10 W green LED source was used as the irradiation source in this study. The mixture of the photocatalyst and contaminant was irradiated for 2 hour and absorbance data were collected continuously using an ocean optics high resolution spectrometer through a computer interface. The percentage degradation (%DE) of MB was determined using eqn (11):

$$\%DE = \frac{I_0 - I}{I_0} \times 100 \quad (11)$$

where I_0 is the initial absorption intensity of MB at $\lambda_{\max} = 660$ nm and I is the absorption intensity after 2 hours of continuous photo-irradiation.

In order to establish the surface catalysis mechanism, the Langmuir–Hinshelwood model is applied in MB degradation. The Langmuir–Hinshelwood equation can describe the dependence of [MB] on the degradation rates:

$$R_0 = \frac{dC}{dt} = \frac{k_{L-H}KC_0}{1 + KC_0} \quad (12)$$

where C_0 is the initial concentration of the MB solution, t is the irradiation time, k_{L-H} is the Langmuir–Hinshelwood rate constant, and K is the Langmuir adsorption coefficient of the MB molecules. At a lower initial concentration of MB ($KC_0 \ll 1$), eqn (12) can be simplified to an apparent first order equation:

$$R_0 = k_{L-H}KC_0 = k_{app}C_0 \quad (13)$$

where k_{app} is the apparent first-order rate constant. If the initial concentration of MB is sufficiently high ($KC_0 \gg 1$), eqn (12) can be simplified to a zero order rate equation:

$$R_0 = k_{L-H} \quad (14)$$

2.7. Preparation of dichlorofluorescein and ROS measurements

DCFH was prepared^{36,37} from DCFH-DA (dichlorofluorescein diacetate obtained from Calbiochem) by mixing 0.5 mL of 1.0 mM DCFH-DA in methanol with 2.0 mL of 0.01 N NaOH. This deesterification of DCFH-DA proceeded at room temperature for 30 min, and the mixture was then neutralized with 10 mL of 25 mM NaH_2PO_4 , at pH 7.4. This solution was kept on ice in the dark until use. All the measurements were performed in a total volume of 2.0 mL water that contained 10 μL of DCFH solution, protoporphyrin (1 μM), ZnO (125 μM) and PP-ZnO (individual concentrations of PP and ZnO in the nanohybrid are 1 μM and 125 μM respectively).

2.8. Fabrication of a photo-cell for the photocurrent and IPCE measurements

Photocurrent measurements were done in a dye-sensitized solar cell (DSSC) set-up. For the fabrication of DSSCs, platinum NPs deposited on FTO substrates were used as counter electrodes. The platinum (Pt) nanoparticles were deposited on the

FTO substrates by thermal decomposition of 5 mM platinum chloride, H_2PtCl_6 , H_2O , Fluka, solution in isopropanol at 385 °C for 30 min. PP coated ZnO NRs were used as the photoelectrodes and the two electrodes were placed on top of each other with a single layer of 50 μm thick surllyn 1702 (Dupont) as a spacer between the two electrodes. A liquid electrolyte composed of 0.5 M lithium iodide (LiI), 0.05 M iodine (I_2) and 0.5 M 4-tertbutylpyridine (TBP) in acetonitrile was used as the hole conductor and filled in the inter-electrode space by using capillary force, through two small holes (diameter = 1 mm) pre-drilled on the counter electrode. Finally, the two holes were sealed by using another piece of surllyn to prevent the leakage of electrolyte from the cell.

2.9. Bacterial strain and culture conditions

The viable count assay was performed with *E. coli* XL1-Blue cells. The cells were cultured at 37 °C in a liquid Luria-Bertani (LB) medium. When the optical density reached 0.6, the inoculum was serially diluted ten thousand times with a Luria-Bertani (LB) medium and plated in LB agar plates containing protoporphyrin (0.2 μM), ZnO (25 μM) and PP-ZnO (individual concentrations of PP and ZnO in the nanohybrid are 0.2 μM and 25 μM respectively). The amount of PP on the ZnO surface was quantified from the absorption spectrum of PP-ZnO nanohybrids after the baseline correction. The PP concentration is calculated from the Q bands around 640 nm as ZnO has no absorbance above 380 nm. In order to study the effect of light, the plates were then incubated at 37 °C for three hours and kept under green light ($\sim 500 \text{ Wm}^{-2}$) for one hour. Finally, the colonies were counted after overnight incubation.

3. Results and discussion

A typical high-resolution transmission electron microscopic (HR-TEM) image of ZnO NPs is shown in Fig. 1a. The lattice fringe of ZnO NP shows an interplanar distance of ~ 0.26 nm, corresponding to the spacing between two (002) planes. The average particle size is estimated by fitting our experimental TEM data over 60 particles and it is found to be ~ 5 nm. As characterized by UV-Vis spectroscopy, the Soret band peak of drug PP resides at 405 nm while the Q-band peaks are observed in the range between 500 nm and 650 nm as shown in Fig. 1b. The Soret band of PP-ZnO is red-shifted by ~ 5 nm as compared to that of free PP. The bathochromic shift of the Soret band is related to different physical and chemical changes in the porphyrin molecular structure when it is incorporated into solids or, under specific conditions, in solution. This observation suggests successful anchoring of PP to the ZnO surface. The efficiency of the ZnO NPs as nanodelivery vehicles is also evident from our UV-Vis spectroscopic studies. The absorption spectra of ZnO NPs as shown in Fig. 1b have baseline upliftment due to the scattering of colloidal ZnO NPs. The ZnO NPs have no molecular absorption beyond 380 nm. According to the Rayleigh scattering, the scattering intensity is inversely proportional to the fourth order of wavelength offering a higher

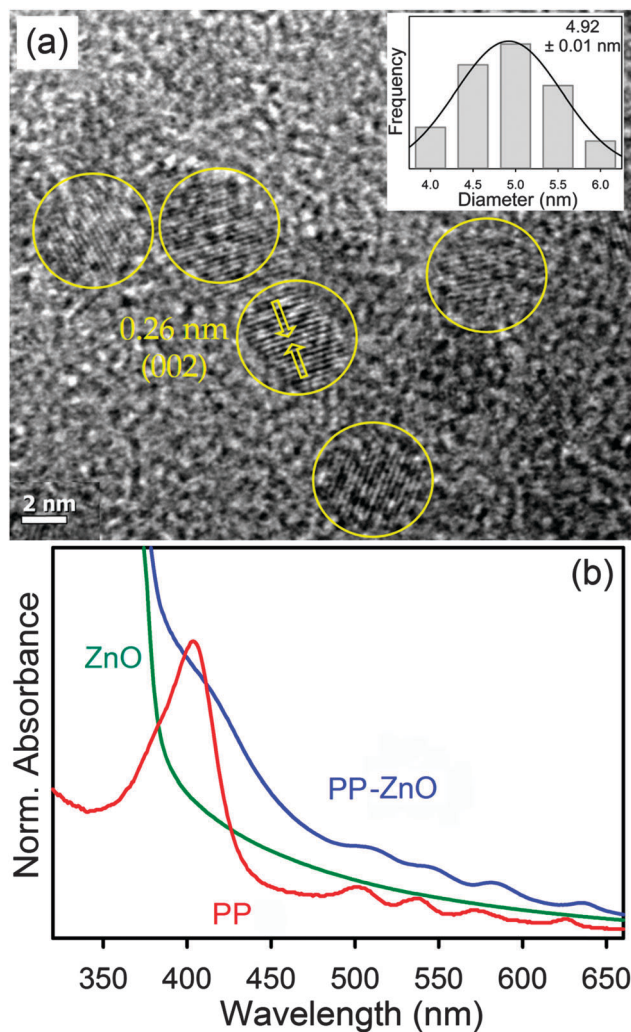


Fig. 1 (a) HRTEM images of ZnO NPs. Inset shows the size distribution of the ZnO NPs. (b) UV-Vis absorption of ZnO NPs (green), PP (red) and PP-ZnO (blue) in the DMSO-ethanol mixture.

scattering cross section of the colloidal samples at a lower wavelength. Thus the baseline upliftment in the absorption spectra (Fig. 1b) decreases with increase in the wavelength. We have estimated that 74 μM and 20 μM of PP are associated with 9.6 nM and 4.2 nM of 5 nm and 30 nm ZnO NPs respectively.³⁸ In other words ~ 7800 and ~ 5000 PP are found to be attached with each 5 nm and 30 nm ZnO NPs respectively.

The Fourier transform infra-red (FTIR) technique is used to investigate the binding mode of the carboxylate group of PP on the ZnO surface as the attachment is very crucial for precise and safe delivery of the drug. For free PP, stretching frequencies of the carboxylic group are at 1695 cm^{-1} and 1406 cm^{-1} for antisymmetric and symmetric stretching vibrations, respectively, as shown in Fig. 2a. When PP is attached to ZnO, the stretching frequencies of the carboxylic group are located at 1604 cm^{-1} and 1418 cm^{-1} for antisymmetric and symmetric stretching vibrations, respectively. The shifting of the stretching frequencies clearly indicates the formation of a covalent bond between the drug PP and the carrier ZnO NPs.^{39–41} The difference between

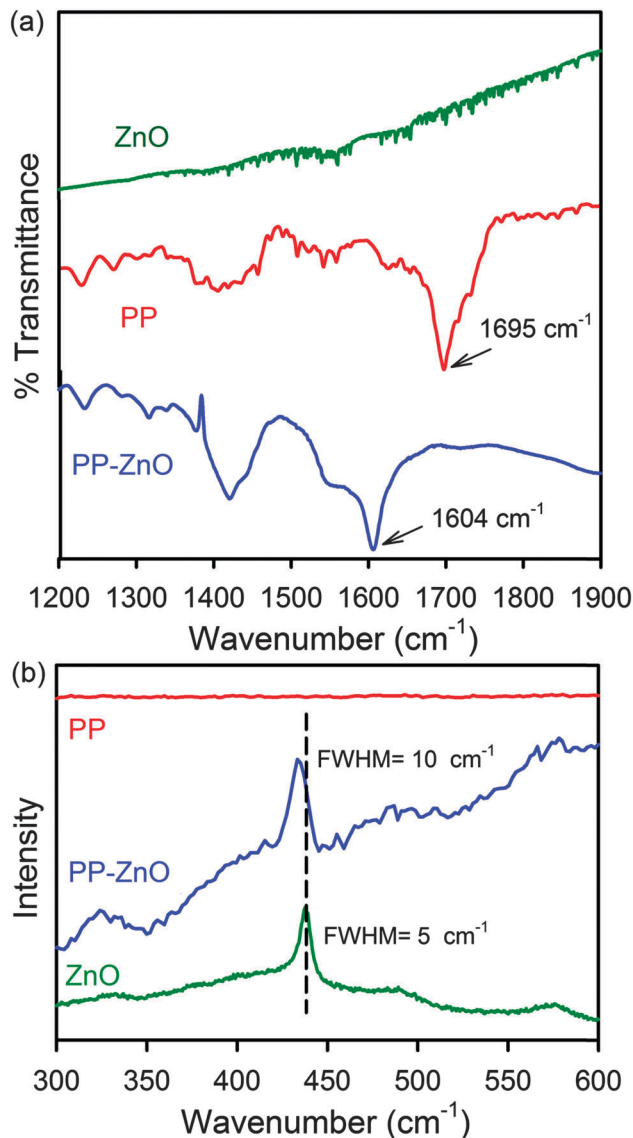


Fig. 2 (a) FTIR and (b) Raman spectra of PP (red), ZnO NPs (green) and PP-ZnO composites (blue).

carboxylate stretching frequencies $\Delta = \nu_{\text{as}} - \nu_{\text{sym}}$ is useful in identifying the bonding mode of the carboxylate ligand.⁴² The observed Δ value for the hybrid material is 186 cm^{-1} which is smaller than that of free PP (289 cm^{-1}). This observation is consistent with the fact that the binding mode of PP on the ZnO surface is predominantly bidentate. To further investigate the binding between the drug and delivery vehicle, Raman spectra were collected from PP, ZnO NPs and PP-ZnO nanohybrids as shown in Fig. 2b. The Raman spectrum of PP does not show any peak in the wavenumber range of 300–600 cm^{-1} . However, four vibration peaks at 328, 378, 438, and 577 cm^{-1} are observed in the Raman spectrum of ZnO NPs, indicating the presence of a wurtzite structure. After binding of PP on the ZnO surface, the characteristic bands of ZnO are all present but slightly blue shifted and broadened, which is indicative of their good retention of the crystal structure and shape. The strong peak at 438 cm^{-1} is

assigned to the nonpolar optical phonon, E_2 mode of the ZnO NPs at high frequency, which is associated with oxygen deficiency. Noticeably, the E_2 mode's characteristic band of ZnO shifts toward lower wavenumbers and its linewidth is larger upon its attachment to PP. The observation can be attributed to the attachment of the carboxylic group to Zn(II) that is located at the ZnO surface.

The room temperature PL spectrum of ZnO NP is comprised of two emission bands upon excitation above the band-edge ($\lambda_{\text{ex}} = 300$ nm) as shown in Fig. 3a. The narrow UV band centered at 363 nm in the emission spectra of ZnO NPs is due to the band gap emission. The broad emission in the blue green region is due to defect centers located near the surface. The broad emission is composed of two bands: one arises from the doubly charged vacancy center (V_{o}^{++}) located at 555 nm (P_2) and the other arises from the singly charged vacancy center (V_{o}^+) located at 500 nm (P_1).^{43,44} The emission intensity of ZnO NPs in the PP-ZnO nanohybrid decreases considerably than

that of free ZnO NPs which can be attributed to the efficient non-radiative photoinduced processes from ZnO NPs to PP. Herein, we propose Förster resonance energy transfer (FRET) from the donor ZnO NPs to the acceptor PP. The assessment of molecular distances in numerous biomolecular assemblies from FRET calculations has become a very useful tool.^{35,45,46} The spectral overlap of the donor ZnO NP emission with that of the PP absorption is shown in Fig. 3b. The fluorescence decay profile of the donor ZnO NPs in the presence and absence of the acceptor PP was obtained upon excitation of a 375 nm laser and monitored at 500 nm (P_1) and 555 nm (P_2) (Fig. 3c and d, respectively). The excited state lifetime of the ZnO NPs quenches in the PP-ZnO nanohybrid compared to that of bare ZnO NPs. The details of the spectroscopic parameters and the fitting parameters of the fluorescence decays are tabulated in Table 1. From FRET calculations, the distance between the donor ZnO NPs and acceptor PP drug are determined to be 1.59 nm and 1.16 nm for P_1 and P_2 states respectively. The energy transfer

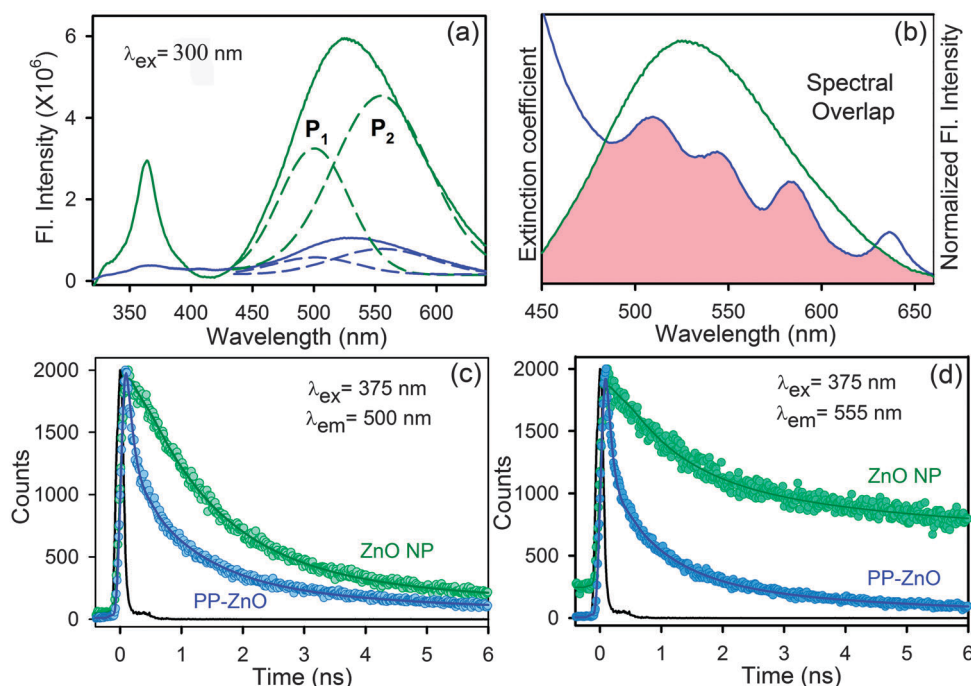


Fig. 3 (a) Room temperature PL spectra of ZnO NPs (green) and PP-ZnO composites (blue) are shown. The excitation wavelength was at 300 nm. The broad emission band is composed of two components, P_1 (500 nm) and P_2 (555 nm). (b) Shows the overlap of the ZnO NP emission and PP absorption. The picosecond-resolved fluorescence transients of ZnO NPs (excitation at 375 nm) in the absence (green) and in the presence of PP (blue) collected at (c) 500 nm and (d) 555 nm are shown.

Table 1 Dynamics of picosecond-resolved luminescence transients of PP and PP-ZnO composites^a

Sample	Excitation wavelength (nm)	Detection wavelength (nm)	τ_1 (ns)	τ_2 (ns)	τ_3 (ns)	τ_{avg} (ns)
ZnO NP	375	500	1.14 ± 0.06 (67.4%)	2.41 ± 0.04 (27.0%)	38.94 ± 0.71 (5.6%)	3.60 ± 0.11
PP-ZnO nanohybrid	375	500	0.11 ± 0.03 (65.7%)	1.04 ± 0.03 (27.1%)	6.27 ± 0.12 (7.2%)	0.80 ± 0.03
ZnO NP	375	555	0.95 ± 0.03 (50.7%)	3.90 ± 0.23 (21.3%)	44.76 ± 0.56 (28.0%)	13.84 ± 0.21
PP-ZnO nanohybrid	375	555	0.08 ± 0.04 (71.3%)	0.87 ± 0.03 (21.3%)	4.81 ± 0.11 (7.4%)	0.60 ± 0.03

^a Numbers in the parenthesis indicate relative weightages.

efficiency is calculated to be 77.7% and 95.7% from P_1 and P_2 states respectively. The FRET distances confirm the proximity of the PP drugs to the ZnO NP delivery vehicle.

In order to explore PP as an efficient source of electrons, a well-known electron acceptor benzoquinone (BQ) is attached to PP and the possible excited-state electron donor-acceptor interactions in the PP-BQ composite are investigated by a series of time-resolved fluorescence measurements with increasing BQ concentrations. The fluorescence decay profile for PP-BQ and free PP was obtained upon photoexcitation at 409 nm in DMSO and monitored at 630 nm as shown in Fig. 4a. The time profile of the fluorescence decay at 630 nm for the singlet excited-state of reference PP showed single exponential decay, with a lifetime of 16.09 ns. The lifetime components of the transients are tabulated in Table 2. As evident from Table 2, time components of ~ 1.50 ns and ~ 0.14 ns appear in the fluorescence transients of PP in the presence of the quencher. These components were found to be enhanced with an increase in BQ concentrations. The fast-decaying component of ~ 140 ps in the PP-BQ composite accounts for the ultrafast charge transfer process from PP to electron acceptor BQ molecules. The time component

Table 2 Dynamics of picosecond-resolved luminescence transients of PP in the absence and presence of various BQ concentrations^a

Sample	τ_1 (ns)	τ_2 (ns)	τ_3 (ns)	τ_{avg} (ns)
PP (bare)			16.09 (100%)	16.09
PP-BQ (1.0 nM)	0.136 (19%)	1.50 (9%)	13.5 (72%)	10.46
PP-BQ (2.0 nM)	0.136 (43%)	1.50 (19%)	13.5 (38%)	5.47
PP-BQ (3.6 nM)	0.136 (49%)	1.50 (22%)	13.5 (29%)	4.75
PP-BQ (5.1 nM)	0.136 (54%)	1.50 (27%)	13.5 (19%)	3.19

^a The emission (monitored at 630 nm) was detected with 409 nm laser excitation. Numbers in the parenthesis indicate relative weightages.

of ~ 1.50 ns appears probably due to the formation of PP aggregates in the experimental solution.⁴⁷ The PL quenching, as evident from the time-resolved PL studies, shows the affinity of PP dyes to BQ molecules. A detailed Stern-Volmer (SV) analysis on the quenching of the PP PL (as shown in Fig. 4b) reveals the dynamic quenching constant to be $K_D = 7.3 \times 10^8 \text{ M}^{-1} \text{ s}^{-1}$. After highlighting the photoinduced charge migration pathway as one of the key aspects of a potential PS in the presence of organic molecules, it is necessary to understand the charge separation dynamics at the PP-ZnO interface to realize a superior ROS activity. Upon 409 nm photoexcitation, the strong fluorescence intensities of PP in the range of 620–720 nm were significantly suppressed when anchored to ZnO NPs as shown in Fig. 5a. In addition, the fluorescence peak of PP in the PP-ZnO nanohybrids was found to be red-shifted by ~ 5 nm as compared to the fluorescence spectra of free PP. The observation is indicative of electronic interaction between the singlet excited state of PP and ZnO NPs. The fluorescence decays (Fig. 5b) of PP, PP-ZnO (5 nm) and PP-ZnO (30 nm) were measured upon excitation with a 409 nm laser, and monitored at a wavelength of 630 nm. The spectroscopic and fitting parameters are shown in Table 3. The longer lifetime of PP quenches in the presence of both ZnO (5 nm) and ZnO (30 nm) NPs. The observed decrease in lifetime could be correlated with the electron transfer process from PP to ZnO NPs. The apparent rate constant, k_{nr} , is determined for the nonradiative processes by comparing the lifetimes of PP in the absence (τ_0) and the presence (τ) of ZnO NPs, using the following equation:

$$k_{\text{nr}} = 1/\langle\tau\rangle - 1/\langle\tau_0\rangle$$

The apparent rate constant for the nonradiative process was estimated to be $1.75 \times 10^9 \text{ s}^{-1}$ for PP-ZnO (5 nm) and $1.70 \times 10^8 \text{ s}^{-1}$ for PP-ZnO (30 nm) adducts. As reported in previous studies,⁴⁰ such k_{nr} values represent electron transport from the LUMO of PP to the conduction band of ZnO NPs. The observations rule out the possibility of self-quenching due to the aggregation of PP molecules on the ZnO surface.^{48–50}

A transmission electron microscopy (TEM) image of PP-ZnO (~ 30 nm) nanohybrids dispersed in water confirms the presence of nearly spherical nanocrystals as shown in Fig. 6a. The HR-TEM image of ZnO NPs shows an interplanar distance of ~ 0.26 nm, corresponding to the spacing between two (002) planes as shown in Fig. 6a, inset. The dynamic light scattering (DLS) spectra of PP-ZnO nanohybrids and ZnO NPs dispersed in water are

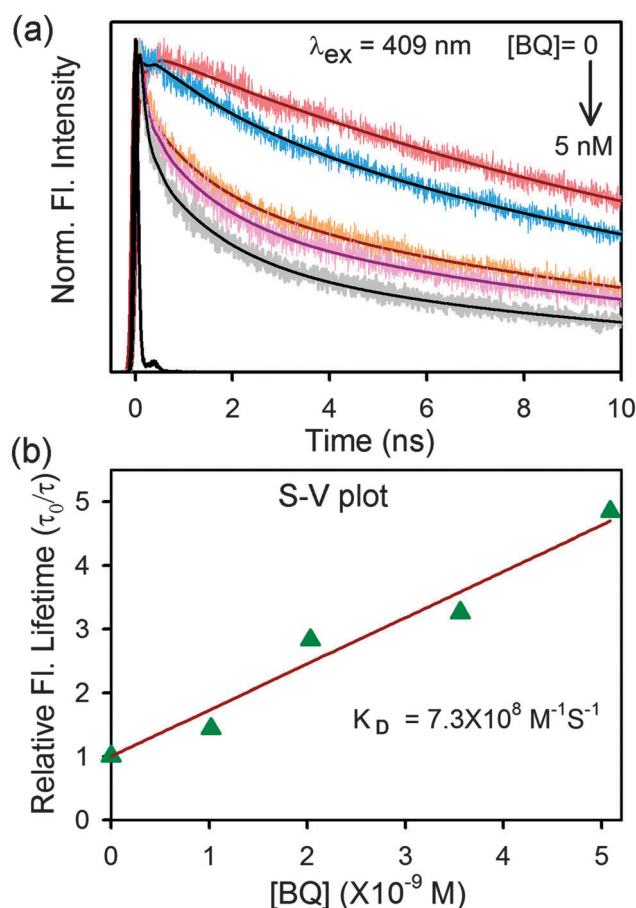


Fig. 4 (a) Fluorescence decay profiles of PP in DMSO with increasing concentrations of BQ (1.0, 2.0, 3.6, and 5.1 nM). (b) Plots of τ_0/τ vs. BQ concentration, where τ_0 and τ represent the excited-state lifetime of the fluorophore (PP) at 630 nm in the absence and presence of quencher (BQ), respectively. Excitation wavelength (λ_{ex} = 409 nm).

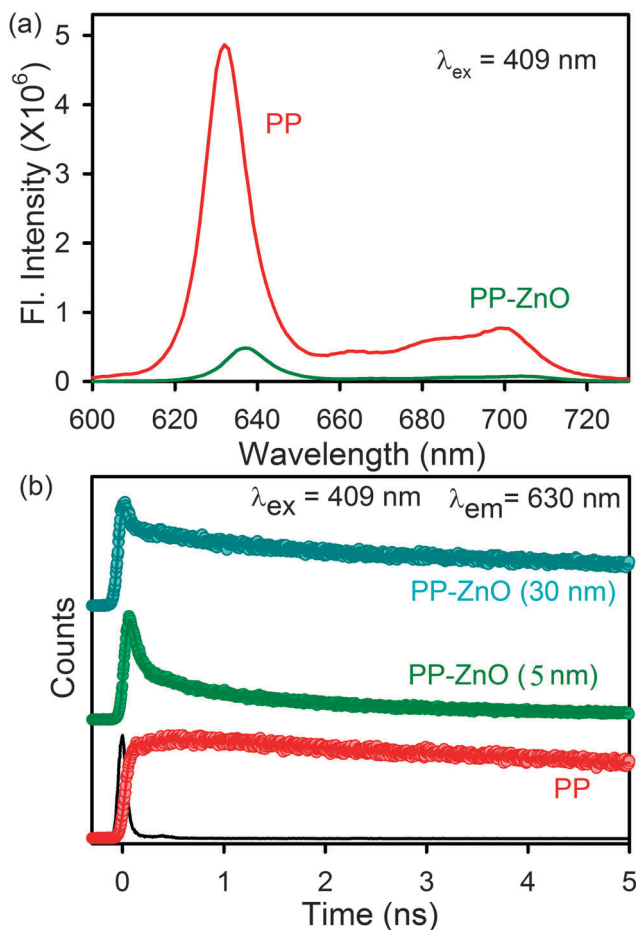


Fig. 5 (a) Room-temperature PL spectra (excitation at 409 nm) of free PP (red) and PP-ZnO (green). (b) Fluorescence decay profiles of PP (red), PP-ZnO (5 nm) (blue) and PP-ZnO (30 nm) (cyan) at 630 nm (excitation at 409 nm).

shown in Fig. 6b. ZnO NPs show a peak at 40 nm which is consistent with TEM results and a peak at 300 nm due to the aggregation in water. The DLS spectra remain almost similar when ZnO NPs are attached to the PP drug molecules. The observation indicates the formation of stable dispersion of PP-ZnO nanohybrids in water. The time dependent stability of the PP-ZnO nanohybrid dispersion in water is monitored at different pH values (Fig. 7a). The dispersion is less stable in acidic aqueous solution (pH = 5) compared to that in neutral (pH = 7) solution. As the cancer cells are generally acidic in nature, nanohybrids are expected to be deposited more in the cancer cells rather in the normal cells. The dissolution of the nanohybrids at different pH values is also monitored as shown

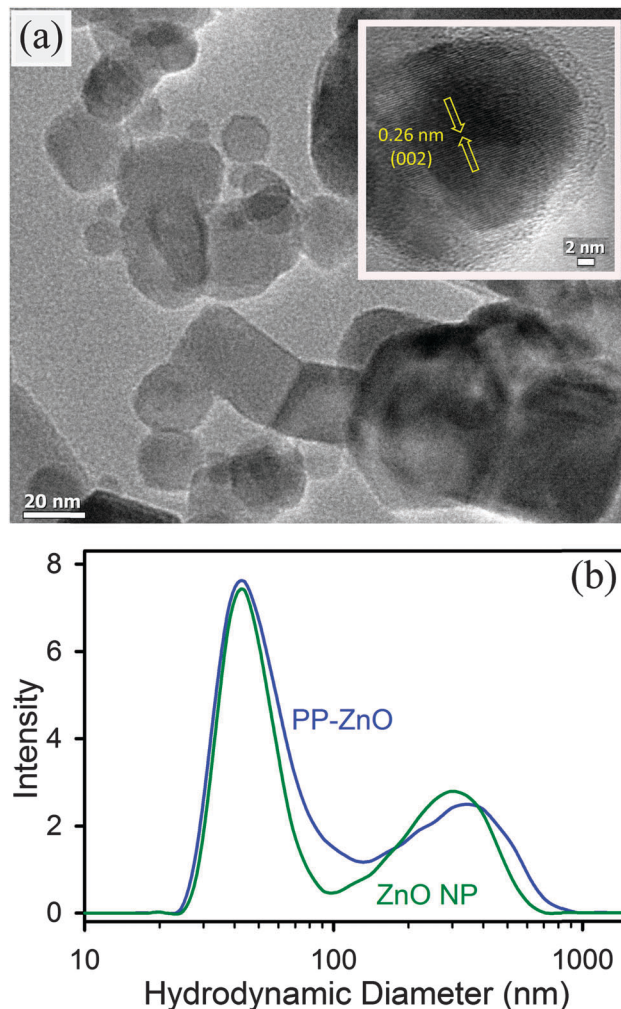


Fig. 6 (a) TEM images of PP-ZnO (~30 nm) nanohybrids dispersed in water. Inset shows the HRTEM image of a PP-ZnO nanohybrid. (b) Dynamic light scattering spectra for PP-ZnO and ZnO NPs dispersed in water.

in Fig. 7a, inset. At pH 5, 8% PP-ZnO nanohybrids were dissolved, whereas, 3% dissolution occurs at pH 7 after 12 hours. The ROS generation was monitored directly by the dichlorofluorescein-dichlorofluorecein (DCFH-DCF) conversion in aqueous medium. The DCFH is a well-known marker for ROS detection.³⁶ ROS oxidize nonfluorescent DCFH to fluorescent DCF and the emission intensity of DCF was monitored with time as shown in Fig. 7b. In the presence of PP-ZnO nanohybrids, maximum enhancement in fluorescence intensity was observed under green light irradiation. In a control experiment ZnO NPs show no ROS generation under green light illumination as the NPs

Table 3 Dynamics of picosecond-resolved luminescence transients of PP and PP-ZnO composites^a

Sample	τ_1 (ns)	τ_2 (ns)	τ_3 (ns)	τ_{avg} (ns)	$k_{\text{nr}} \times 10^9$ (s ⁻¹)
PP (bare)			16.09 (100%)	16.09	
PP-ZnO (5 nm), nanohybrid	0.06 ± 0.03, (76.3%)	0.71 ± 0.03, (13.4%)	4.00 ± 0.08, (10.3%)	0.55 ± 0.09	1.75
PP-ZnO (30 nm), nanohybrid	0.05 ± 0.03, (58.8%)	0.93 ± 0.04, (10.6%)	13.35 ± 0.17, (30.6%)	4.21 ± 0.06	0.17

^a The emission (monitored at 630 nm) was detected with 409 nm laser excitation. k_{nr} represents the nonradiative rate constant. Numbers in the parenthesis indicate relative weightages.

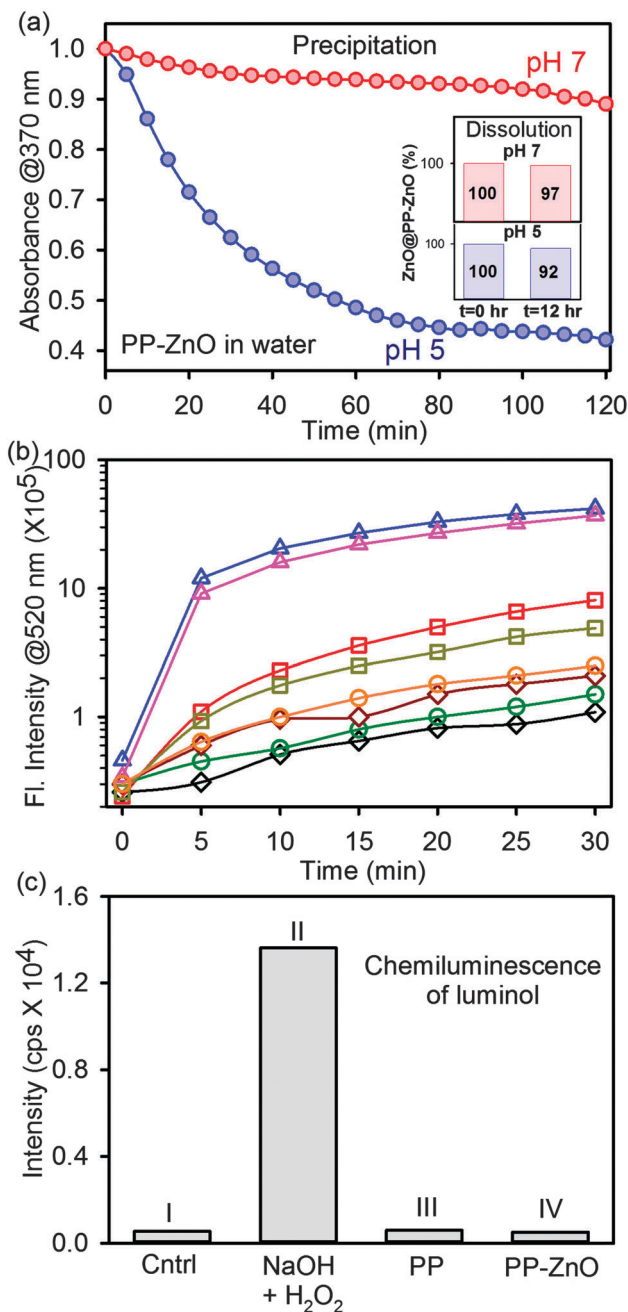


Fig. 7 (a) Stability of the nanohybrid from absorbance at 370 nm of PP-ZnO dispersed in water at pH 7 and pH 5. Inset shows the dissolution of PP-ZnO nanohybrids in water at pH 5 and pH 7 after 12 hours. (b) The DCFH oxidation with time in the presence of PP-ZnO (blue at pH 5 and pink at pH 7), PP (red at pH 5 and dark yellow at pH 7), ZnO (green at pH 5 and orange at pH 7) and DCFH only (black at pH 5 and dark red at pH 7) under green light irradiation. The excitation was at 488 nm. (c) Chemiluminescence of luminol after green light irradiation for 15 minutes in the presence of (I) control, (II) NaOH + H₂O₂, (III) PP and (IV) PP-ZnO.

lack photon absorption in the green region of the optical spectrum. Thus ZnO NPs in the proximity of PP drugs not only act as drug delivery vehicles as reported in the literature but also enhance the generation of ROS. The ROS generation by the nanohybrid in acidic aqueous solution (pH 5) compared with

that in neutral pH = 7 is monitored by DCFH oxidation and found to be comparable as shown in Fig. 7b. It has to be noted that DCFH oxidation is not conclusive to confer the nature of ROS (singlet oxygen/superoxide formation). However, in the presence of superoxide, more specifically, luminol is oxidized to produce chemiluminescence.⁵¹ As shown in Fig. 7c, no chemiluminescence observed in the presence of PP and PP-ZnO after green light irradiation for 15 minutes. The above observations of DCFH oxidation and no oxidation of luminol in PP/PP-ZnO nanohybrids upon green light illumination indicate that the nature of ROS is essentially singlet oxygen rather superoxide anions. The conclusion of the formation of singlet oxygen is consistent with the reported literature as Carraro *et al.* have shown that photosensitized reactions *in vitro* and *in vivo* by porphyrin involve the production of ¹O₂ but not O₂⁻ or •OH radicals.⁵²

A well known dye methylene blue (MB) is reported to be bleached to Leuco-methylene blue (LMB) in the presence of ROS in several photocatalysis experiments.^{53,54} However, under green light irradiation, in the presence of PP-ZnO nanohybrids, 30% MB is reduced to Leuco methylene blue (LMB) whereas no MB reduction occurs in the presence of PP only (Fig. 8). The observation along with the conclusion made earlier clearly indicates that MB reduction in the present case is neither through singlet oxygen nor through superoxide formation. The efficacy of direct electron transfer of PP to BQ (Fig. 4) is assigned to be responsible for the MB reduction in the nanohybrid as shown in Fig. 8a. It has to be noted that the proximity of MB to PP (precondition for direct electron transfer) without ZnO is hindered because of higher solubility of MB in aqueous solution. In the present PP sensitization approach, the photo-excited dye molecule transfers an electron into the conduction band (CB) of ZnO, thereby enhancing the charge separation at the dye-semiconductor interface. MB is reduced to LMB by taking the electron from ZnO CB. Concurrently water in the media acts as an electron donor to regenerate the sensitizer dye.³⁹ To confirm the surface catalysis mechanism, MB reduction is performed in the presence of PP-ZnO by varying the initial MB concentration. The MB degradation rate (R_0) versus the initial MB concentration (C_0) curve as shown in Fig. 8c is fitted using the Langmuir-Hinshelwood equation. The values of K and k_{L-H} are given in Table 4 and are consistent with other surface catalyzed reactions.³⁹

The evidence for electron transfer from PP dye to the host ZnO NP is apparent from an incident photon-to-current conversion efficiency (IPCE) measurement in a photocell as shown in Fig. 9a. The SEM images of ZnO NRs used in the photocell are shown in Fig. 9b. The light source (intensity 25 mW cm⁻²) was turned on and off every 20 s, and the obtained current values were continuously recorded using a multimeter. The inset of Fig. 9c shows the photocurrent response for the ZnO NR and PP-ZnO thin films, where an improved photocurrent was observed for the PP-modified ZnO thin film (~100 μA) under illuminated conditions compared to the bare ZnO NR thin film (~10 μA). The incident photon-to-current conversion efficiency (IPCE) of the device as shown in Fig. 9c is found to be closely identical to absorbance spectra of PP and as large as 40% at 395 nm. This shows that the PP sensitizers on the photo

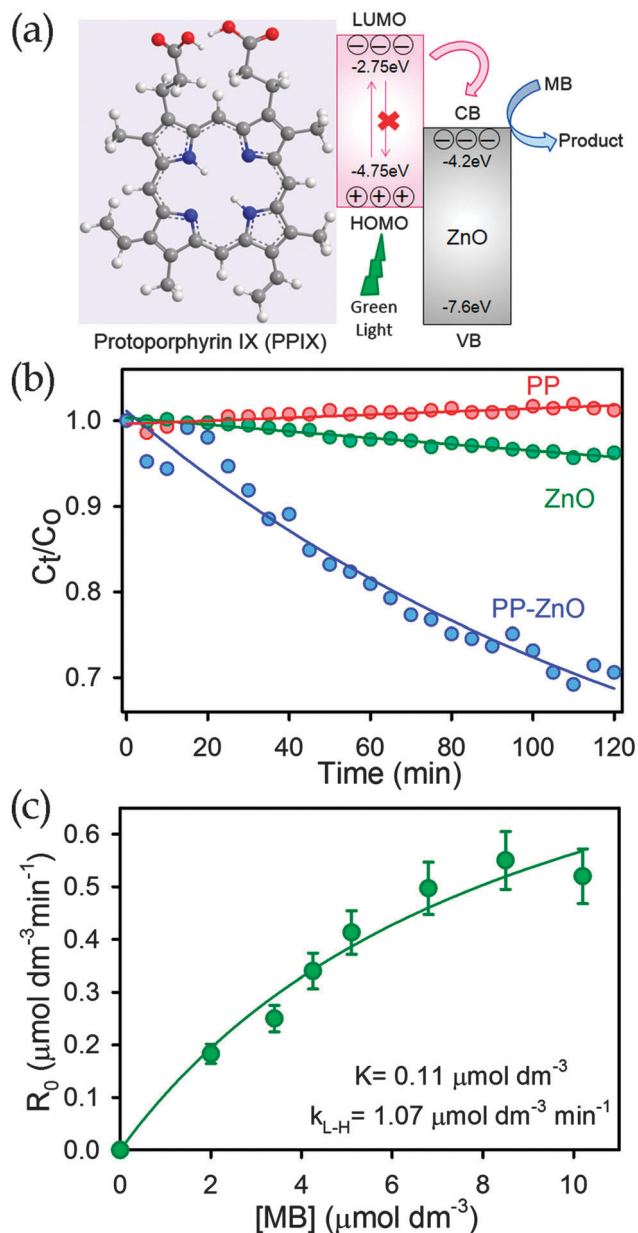


Fig. 8 (a) Schematic energy level diagram and charge separation path in PP-ZnO interface. (b) Photocatalytic degradation of MB in the presence of PP (red), ZnO (green) and PP-ZnO (blue) under green light irradiation. (c) Degradation rate (R_0) versus initial MB concentration (C_0) plots (with 10% error bar) in the presence of PP-ZnO under green light irradiation.

Table 4 Kinetic fitting parameters of the Langmuir-Hinshelwood model^a

Sample	$[\text{MB}]$ ($\mu\text{mol dm}^{-3}$)	R_0 ($\mu\text{mol dm}^{-3} \text{min}^{-1}$)	K ($\mu\text{mol dm}^{-3}$)	k_{L-H} ($\mu\text{mol dm}^{-3} \text{min}^{-1}$)
PP-ZnO	2.0000	0.1830	0.11	1.07
	3.4000	0.2500		
	4.2500	0.3400		
	5.1000	0.4130		
	6.8000	0.4970		
	8.5000	0.5500		
	10.2000	0.5200		

^a R_0 is the degradation rate, k_{L-H} is the Langmuir-Hinshelwood rate constant, and K is the Langmuir adsorption coefficient.

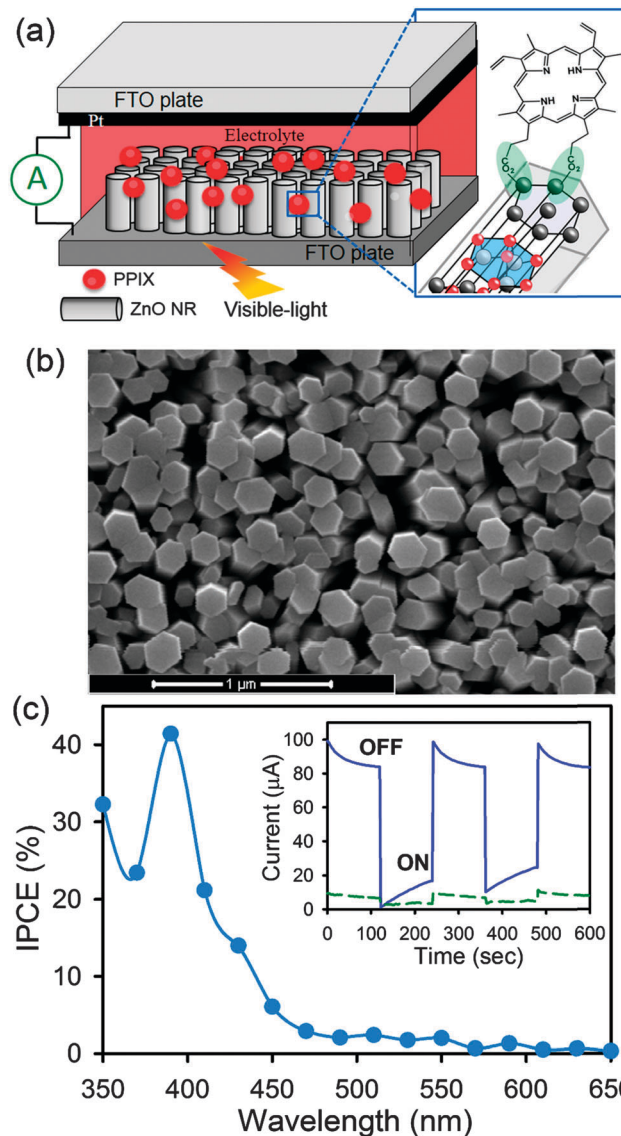


Fig. 9 (a) Schematic presentation of the fabricated dye sensitized solar cell geometry for photocurrent measurement. (b) SEM images of vertically aligned, hexagonal ZnO NRs decorated on a FTO plate. (c) Incident photon-to-current conversion efficiency (IPCE) spectra for PP-sensitized ZnO NRs.

anode surface are indeed responsible for the photocurrent generation.

After thorough characterization and investigation of photo-induced dynamics in PP-ZnO nanohybrids, we have employed the PP-ZnO nanohybrids as potential photodynamic agents for the inhibition of growth of *Escherichia coli* (*E. coli*). For photodynamic therapy experiments, we have used 30 nm ZnO NPs due to lower toxicity than that of 5 nm ZnO NPs.⁵⁵ Fig. 10b shows the picture of *E. coli* cultures treated with PP-ZnO nanohybrids in the presence and absence of green light. The inhibition of bacterial growth after photodynamic treatment is clearly visible. The green light treated sample contains significantly less number of colonies. For comparison, the colonies were counted for control and treated with PP drugs, ZnO NPs and PP-ZnO

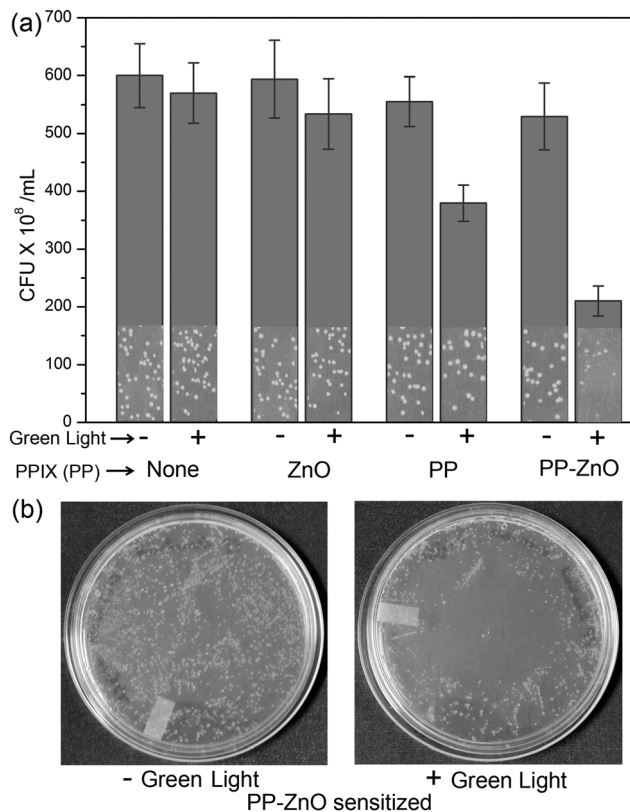


Fig. 10 (a) Antibacterial activity of PP-ZnO, PP and ZnO in the presence and absence of green light. (b) Images of *E. coli* in PP-ZnO sensitized plates before and after green light irradiation.

nanohybrids in the presence and absence of green light as shown in Fig. 10a. The images of the selected area for the corresponding samples are shown within the columns in the Fig. 10a. In control and ZnO treated samples, the colony forming units (CFU) are almost same in the presence and absence of green light. The observation indicates the absence of antibacterial activity of the ZnO NP itself in our experimental concentration range. In the case of PP treated samples, the bacteria growth is inhibited up to 34% after photodynamic treatment. The maximum inhibition of bacterial growth is obtained for PP-ZnO treated samples where a 65% decrease in CFU is observed after photodynamic treatment. The results clearly indicate the enhanced ROS generation in the presence of PP-ZnO nanohybrids compared to that of PP only as the presence of ZnO NPs in the proximity of PP drugs facilitates the charge separation which is evident from our picosecond resolved fluorescence studies.

4. Conclusion

We have investigated the crucial photoinduced dynamics in ZnO nanoparticles (NPs) upon complexation with the cancer drug protoporphyrin IX (PP). Association of ~ 7800 and ~ 5000 PP molecules per 5 nm and 30 nm ZnO NPs, respectively, is evidenced from our study. The PP-ZnO nanohybrid was characterized by vibrational spectroscopy (FTIR), Raman scattering and UV-Vis

absorption spectroscopy. To confirm the proximity of the drug and vehicle of delivery at the molecular level, we have employed picosecond-resolved Förster resonance energy transfer (FRET) from the defect mediated emission of ZnO NPs to PP and the distance between the two is found to be 1.16 nm from P₂ states. Picosecond-resolved fluorescence studies on PP-ZnO nanohybrids also reveal efficient electron migration from photoexcited PP to ZnO, eventually enhancing the ROS activity in the PP-ZnO nanostructures. The dichlorofluorescein (DCFH) oxidation and no oxidation of luminol in PP/PP-ZnO nanohybrids upon green light illumination indicate that the nature of ROS is essentially singlet oxygen rather superoxide anions. The photocurrent and incident photon-to-current conversion efficiency (IPCE) measurements confirm the enhanced charge separation in PP-ZnO nanohybrids under photoirradiation. The nanohybrid shows greater photodynamic activity for the inhibition of *E. coli* growth compared to that of free drug molecules. The exploration of key photoinduced dynamics in the porphyrin based nanohybrids will be helpful in designing future photodynamic agents.

Acknowledgements

S. C and P. K. thank CSIR (India) for research fellowship. We thank DST (India) for financial grants DST/TM/SERI/2k11/103 and SB/S1/PC-011/2013. We also thank DAE (India) for financial grant 2013/37P/73/BRNS. PL thanks the NTH-School "Contacts in Nanosystems: Interactions, Control and Quantum Dynamics", the Braunschweig International Graduate School of Metrology, and DFG-RTG 1953/1, Metrology for Complex Nanosystems.

References

- 1 J. Park, P. M. Fong, J. Lu, K. S. Russell, C. J. Booth, W. M. Saltzman and T. M. Fahmy, *Nanomedicine*, 2009, **5**, 410–418.
- 2 X. Wang, J. Li, Y. Wang, L. Koenig, A. Gjyzezi, P. Giannakakou, E. H. Shin, M. Tighiouart, Z. Chen, S. Nie and D. M. Shin, *ACS Nano*, 2011, **5**, 6184–6194.
- 3 L. Brannon-Peppas and J. O. Blanchette, *Adv. Drug Delivery Rev.*, 2004, **56**, 1649–1659.
- 4 E. S. Kawasaki and A. Player, *Nanomedicine*, 2005, **1**, 101–109.
- 5 L. Zhang, F. X. Gu, J. M. Chan, A. Z. Wang, R. S. Langer and O. C. Farokhzad, *Clin. Pharmacol. Ther.*, 2008, **83**, 761–769.
- 6 R. A. Petros and J. M. DeSimone, *Nat. Rev. Drug Discovery*, 2010, **9**, 615–627.
- 7 L. Gao, J. Fei, J. Zhao, H. Li, Y. Cui and J. Li, *ACS Nano*, 2012, **6**, 8030–8040.
- 8 K. Wang, Q. He, X. Yan, Y. Cui, W. Qi, L. Duan and J. Li, *J. Mater. Chem.*, 2007, **17**, 4018–4021.
- 9 T. Jamieson, R. Bakhshi, D. Petrova, R. Pocock, M. Imani and A. M. Seifalian, *Biomaterials*, 2007, **28**, 4717–4732.
- 10 J. L. Pelley, A. S. Daar and M. A. Saner, *Toxicol. Sci.*, 2009, **112**, 276–296.

- 11 N. Singh, B. Manshian, G. J. Jenkins, S. M. Griffiths, P. M. Williams, T. G. Maffei, C. J. Wright and S. H. Doak, *Biomaterials*, 2009, **30**, 3891–3914.
- 12 H.-M. Xiong, *Adv. Mater.*, 2013, **25**, 5329–5335.
- 13 K. C. Barick, S. Nigam and D. Bahadur, *J. Mater. Chem.*, 2010, **20**, 6446–6452.
- 14 Q. Yuan, S. Hein and R. D. K. Misra, *Acta Biomater.*, 2010, **6**, 2732–2739.
- 15 M. Fakhar-e-Alam, S. Rahim, M. Atif, M. H. Aziz, M. I. Malick, S. S. Z. Zaidi, R. Suleman and A. Majid, *Laser Phys. Lett.*, 2014, **11**, 039501.
- 16 G. Yang, L. Liu, Q. Yang and S. Wang, *Chem. – Asian J.*, 2011, **6**, 1147–1150.
- 17 T. Lopez, E. Ortiz, M. Alvarez, J. Navarrete, J. A. Odriozola, F. Martinez-Ortega, E. A. Paez-Mozo, P. Escobar, K. A. Espinoza and I. A. Rivero, *Nanomedicine*, 2010, **6**, 777–785.
- 18 M.-R. Ke, J. M. Eastel, K. L. K. Ngai, Y.-Y. Cheung, P. K. S. Chan, M. Hui, D. K. P. Ng and P.-C. Lo, *Chem. – Asian J.*, 2014, **9**, 1868–1875.
- 19 W. E. Grant, A. MacRobert, S. G. Bown, C. Hopper and P. M. Speight, *Lancet*, 1993, **342**, 147–148.
- 20 K. Woodburn and D. Kessel, *J. Photochem. Photobiol., B*, 1994, **22**, 197–201.
- 21 D. C. Hone, P. I. Walker, R. Evans-Gowing, S. FitzGerald, A. Beeby, I. Chambrier, M. J. Cook and D. A. Russell, *Langmuir*, 2002, **18**, 2985–2987.
- 22 M. E. Wieder, D. C. Hone, M. J. Cook, M. M. Handsley, J. Gavrilovic and D. A. Russell, *Photochem. Photobiol. Sci.*, 2006, **5**, 727–734.
- 23 R. Ideta, F. Tasaka, W.-D. Jang, N. Nishiyama, G.-D. Zhang, A. Harada, Y. Yanagi, Y. Tamaki, T. Aida and K. Kataoka, *Nano Lett.*, 2005, **5**, 2426–2431.
- 24 B. Zhao, W. Duan, P.-C. Lo, L. Duan, C. Wu and D. K. P. Ng, *Chem. – Asian J.*, 2013, **8**, 55–59.
- 25 Q. Zou, L. Zhang, X. Yan, A. Wang, G. Ma, J. Li, H. Möhwald and S. Mann, *Angew. Chem., Int. Ed.*, 2014, **53**, 2366–2370.
- 26 W.-D. Jang, N. Nishiyama, G.-D. Zhang, A. Harada, D.-L. Jiang, S. Kawauchi, Y. Morimoto, M. Kikuchi, H. Koyama, T. Aida and K. Kataoka, *Angew. Chem., Int. Ed.*, 2005, **44**, 419–423.
- 27 R. K. Chowdhary, N. Chansarkar, I. Sharif, N. Hioka and D. Dolphin, *Photochem. Photobiol.*, 2003, **77**, 299–303.
- 28 Z.-Y. Zhang, Y.-D. Xu, Y.-Y. Ma, L.-L. Qiu, Y. Wang, J.-L. Kong and H.-M. Xiong, *Angew. Chem., Int. Ed.*, 2013, **52**, 4127–4131.
- 29 A. Makhil, S. Sarkar, T. Bora, S. Baruah, J. Dutta, A. K. Raychaudhuri and S. K. Pal, *Nanotechnology*, 2010, **21**, 265703.
- 30 S. Sarkar, A. Makhil, T. Bora, S. Baruah, J. Dutta and S. K. Pal, *Phys. Chem. Chem. Phys.*, 2011, **13**, 12488–12496.
- 31 S. Sarkar, A. Makhil, S. Baruah, M. A. Mahmood, J. Dutta and S. K. Pal, *J. Phys. Chem. C*, 2012, **116**, 9608–9615.
- 32 S. Baruah and J. Dutta, *J. Cryst. Growth*, 2009, **311**, 2549–2554.
- 33 S. Baruah and J. Dutta, *J. Sol-Gel Sci. Technol.*, 2009, **50**, 456–464.
- 34 S. Sarkar, A. Makhil, K. Lakshman, T. Bora, J. Dutta and S. K. Pal, *J. Phys. Chem. C*, 2012, **116**, 14248–14256.
- 35 J. R. Lakowicz, *Principles of Fluorescence Spectroscopy*, Kluwer Academic/Plenum, New York, 2nd edn, 1999.
- 36 C. P. LeBel, H. Ischiropoulos and S. C. Bondy, *Chem. Res. Toxicol.*, 1992, **5**, 227–231.
- 37 R. Cathcart, E. Schwiers and B. N. Ames, *Anal. Biochem.*, 1983, **134**, 111–116.
- 38 E. S. Jeong, H. J. Yu, S. W. Han, S. J. An, J. Yoo, Y. J. Kim and G. C. Yi, *J. Korean Phys. Soc.*, 2008, **53**, 461–465.
- 39 S. Sardar, S. Sarkar, M. T. Z. Myint, S. Al-Harathi, J. Dutta and S. K. Pal, *Phys. Chem. Chem. Phys.*, 2013, **15**, 18562–18570.
- 40 S. Sarkar, A. Makhil, T. Bora, K. Lakshman, A. Singha, J. Dutta and S. K. Pal, *ACS Appl. Mater. Interfaces*, 2012, **4**, 7027–7035.
- 41 P. Kar, S. Sardar, E. Alarousu, J. Sun, Z. S. Seddigi, S. A. Ahmed, E. Y. Danish, O. F. Mohammed and S. K. Pal, *Chem. – Eur. J.*, 2014, **20**, 10475–10483.
- 42 G. B. Deacon and R. J. Phillips, *Coord. Chem. Rev.*, 1980, **33**, 227–250.
- 43 A. van Dijken, E. A. Meulenkaamp, D. Vanmaekelbergh and A. Meijerink, *J. Phys. Chem. B*, 2000, **104**, 1715–1723.
- 44 K. Vanheusden, W. L. Warren, C. H. Seager, D. R. Tallant, J. A. Voigt and B. E. Gnade, *J. Appl. Phys.*, 1996, **79**, 7983–7990.
- 45 R. M. Clegg, in *Methods Enzymology*, ed. J. E. D. David and M. J. Lilley, Academic Press, 1992, vol. 211, pp. 353–388.
- 46 T. Bora, K. K. Lakshman, S. Sarkar, A. Makhil, S. Sardar, S. K. Pal and J. Dutta, *Beilstein J. Nanotechnol.*, 2013, **4**, 714–725.
- 47 U. Rempel, B. von Maltzan and C. von Borczyskowski, *J. Lumin.*, 1992, **53**, 175–178.
- 48 T. Hasobe, K. Saito, P. V. Kamat, V. Troiani, H. Qui, N. Solladie, K. S. Kim, J. K. Park, D. Kim, F. D'Souza and S. Fukuzumi, *J. Mater. Chem.*, 2007, **17**, 4160–4170.
- 49 H. Saarenpaa, E. Sariola-Leikas, A. P. Perros, J. M. Kontio, A. Efimov, H. Hayashi, H. Lipsanen, H. Imahori, H. Lemmetyinen and N. V. Tkachenko, *J. Phys. Chem. C*, 2012, **116**, 2336–2343.
- 50 H. M. Cheng and W. F. Hsieh, *Nanotechnology*, 2010, **21**, 485202.
- 51 M. M. Tarpey and I. Fridovich, *Circ. Res.*, 2001, **89**, 224–236.
- 52 C. Carraro and M. A. Pathak, *J. Invest. Dermatol.*, 1988, **90**, 267–275.
- 53 C. Yogi, K. Kojima, T. Takai and N. Wada, *J. Mater. Sci.*, 2009, **44**, 821–827.
- 54 S. Lakshmi, R. Renganathan and S. Fujita, *J. Photochem. Photobiol., A*, 1995, **88**, 163–167.
- 55 S. Nair, A. Sasidharan, V. V. Divya Rani, D. Menon, S. Nair, K. Manzoor and S. Raina, *J. Mater. Sci.: Mater. Med.*, 2009, **20**, 235–241.